



# Effects of nanolayer versus nanosphere morphologies on radiative cooling

Ioanna Katsamba<sup>1</sup>, Krutarth Khot<sup>1</sup>, Andrea Felicelli, Xiulin Ruan\*

School of Mechanical Engineering and Birk Nanotechnology Center, Purdue University, 610 Purdue Mall, West Lafayette, 47906, IN, USA

## ARTICLE INFO

### Keywords:

Radiative cooling  
Nanocomposites  
Multilayer structures  
Calcium carbonate (CaCO<sub>3</sub>)  
Monte Carlo  
Transfer matrix method (TMM)

## ABSTRACT

Passive radiative cooling has emerged as a promising solution to address the challenges of energy consumption and climate crisis. Calcium carbonate (CaCO<sub>3</sub>) is a material seen in both cooling paints and snail shells for cooling purposes but with nanoparticle and multilayer morphologies, respectively, raising the question of how the morphology affects the radiative cooling performance. In this work, we calculate the optical performance of the calcite-air nanolayer and nanosphere composites using the Transfer Matrix Method and Mie theory combined with Monte Carlo simulation, respectively. Notably, the nanolayer composite, with a 60% volume fraction, has the maximum reflectance and optimizes at a nanolayer thickness of 300 nm. In comparison, spherical nanoparticles reach their optimum reflectance at around 500–600 nm diameter. Furthermore, nanolayers exhibit higher sky window emissivity of up to 6%, resulting in the highest figure of merit. These results highlight the unique behaviors of each morphology and underscore the need for distinct optimized parameters to achieve high solar reflection.

## 1. Introduction

In recent decades, global warming has become a major concern for the Earth's ecosystem, prompting the exploration of various renewable energy technologies to reduce reliance on fossil fuels. One promising avenue in the fight against climate change is radiative cooling, a passive cooling method that utilizes materials capable of reflecting sunlight strongly (wavelength range 0.25–2.5 μm) and emitting heat effectively into deep space via the sky window (wavelength range 8–13 μm) [1]. This process facilitates surface cooling without the need for electricity consumption, resulting in sub-ambient temperatures. Researchers have made significant strides in developing composites tailored for radiative cooling, such as a commercial titanium dioxide paint layer coated on an aluminum substrate [2], multilayer system of silicon oxide and hafnium oxide [3], a calcium carbonate-acrylic paint [4] and more radiative cooling discoveries [5–11].

While these innovative composites have shown promise in reducing temperatures, the natural world offers intriguing insights as well. Multiple species found in nature manage to cool their bodies due to their complicated structures, e.g., silver ants [12,13], beetles [14], and butterflies [15]. Interestingly, some species of snails, like *Sphincterochila Boissieri* found in Egypt and Israel, have evolved to thrive in extreme environments where ground surface temperatures can reach scorching highs of 65 °C during the summer season [16]. These resilient snails owe their survival to the remarkable radiative cooling properties of

their shells, which are structured in intricate layers [16]. This nanolayer morphology, reminiscent of photonic structures studied extensively in literature [17–21], has recently emerged as a promising avenue for enhancing radiative cooling [22–28].

Interestingly, the CaCO<sub>3</sub> cooling paints [4] and snail shells [16] are two systems both made by calcium carbonate (CaCO<sub>3</sub>), but they employ different morphologies. The question of whether nanolayer structures outperform nanocomposites with spherical particles in practical radiative cooling applications has yet to be definitively addressed through experimental investigations. To bridge this gap, our study harnesses theoretical models and simulations to comprehensively evaluate these two distinct structural approaches. Our goal is to elucidate which morphology holds greater potential for optimizing radiative cooling performance.

In this work, drawing inspiration from the intriguing structure of snail shells, we embark on a comparative analysis of nanolayer structures and nanocomposites featuring spherical particles. Leveraging established computational methods, we employ the transfer matrix method (TMM) for nanolayers and Mie theory in conjunction with Monte Carlo simulations for spherical nanoparticles. These techniques allow us to predict the optical properties of both one-dimensional (1D) multilayer structures and three-dimensional (3D) composites consisting of spherical nanoparticles and enable us to uncover the optimal approach for achieving efficient radiative cooling while maintaining a

\* Corresponding author.

E-mail address: [ruan@purdue.edu](mailto:ruan@purdue.edu) (X. Ruan).

<sup>1</sup> These authors contributed equally.

rigorous and equitable comparison. Parameters such as layer thickness, particle size, and a 60% volume fraction remain the same across both models. Our initial hypothesis postulates that nanolayers may outperform spherical particles due to the bio-inspired structure of snail shells. As we embark on this investigation, we endeavor to address the existing research gap and provide valuable insights into the design and optimization of radiative cooling systems. In the following sections, we will present our methodology for comparative analysis, share our findings, discuss their implications, and conclude with insights into the structure that provides better radiative cooling performance.

## 2. Methods

In this study, we conduct a comparative analysis between two distinct morphologies: the calcite nanosphere-air composite (Fig. 1(a)) and the calcite-air multilayer structure (Fig. 1(b)). The schematic of Fig. 1(a) depicts a nanocomposite consisting of spherical particles inspired by the SEM image of BaSO<sub>4</sub>-Acrylic paint, shown at the bottom, while the schematic of Fig. 1(b) shows a multilayer of two distinct materials, inspired by the SEM image of calcium nanolayers occurring in *Sphincterochila zonata* desert snails. To evaluate their radiative cooling performance comprehensively, we employ a two-pronged approach. Firstly, we utilize the Mie theory combined with the Monte Carlo algorithm (Fig. 1(c)) to assess the optical properties of the spherical nanoparticles, enabling the calculation of crucial parameters such as reflectance, transmittance, and absorptance. Secondly, we turn to the analytical TMM (Fig. 1(d)) to predict the spectral response of the multilayer structure. This dual methodology provides a rigorous and equitable basis for our investigation, allowing us to gain insights into the radiative cooling potential of these structures across various optical parameters.

The models utilized in our study have been extensively validated and are well-established in the literature. For instance, the combination of Mie Theory and the Monte Carlo algorithm has been previously validated, as demonstrated in the work of Li et al. [10], where it exhibited strong agreement with experimental findings. Similarly, the TMM offers an analytical solution to Maxwell's equations for electromagnetic waves within a multilayer structure, with its efficacy reliant on the optical properties of the materials involved. Roy Chowdhury et al. have recently validated the TMM using experimental measurement for thermal barrier coatings [29].

### 2.1. Mie theory

The Mie theory combined with Monte Carlo simulation is used to simulate the nanosphere-air composite. In this work, Mie theory is used to calculate the optical properties of a single spherical particle, such as the scattering and absorption coefficients and the asymmetry parameter. This theory is an analytical solution Gustav Mie developed and considers the correlation between particle cross-section and incident light wavelength ( $\lambda$ ) [30–32].

Calcium carbonate (CaCO<sub>3</sub>) particles are found in multiple shapes [33]. For simplicity, we simulate spherical particles such that only one characteristic length in each system is considered, i.e., the sphere diameter and layer thickness; therefore, a fair comparison is maintained.

Two dimensionless inputs are needed to carry out Mie theory calculations, the complex index of refraction ( $\bar{n} = \frac{n_1 + ik_1}{n_0}$ ) and the size parameter ( $x = \frac{\pi d}{\lambda}$ ), where  $n_0$  and  $n_1$  are the refractive indices of air and calcite,  $\kappa_1$  is the extinction coefficient of calcite and  $d$  is the sphere diameter. By using the two inputs, we can further calculate the Mie coefficients ( $a_i, b_i$ ):

$$\begin{aligned} a_i &= \frac{\bar{n} \psi_i(\bar{n}x) \psi'_i(x) - \psi_i(x) \psi'_i(\bar{n}x)}{n \psi_i(\bar{n}x) \xi'_i(x) - \xi_i(x) \psi'_i(\bar{n}x)}, \\ b_i &= \frac{\psi_i(\bar{n}x) \psi'_i(x) - \bar{n} \psi_i(x) \psi'_i(\bar{n}x)}{\psi_i(\bar{n}x) \xi'_i(x) - \bar{n} \xi_i(x) \psi'_i(\bar{n}x)}. \end{aligned} \quad (1)$$

The terms  $\psi_i$  and  $\xi_i$  represent the Riccati–Bessel functions and  $i$  denotes the function order. The maximum function order is approximated [30] as:  $i_{max} = x + 4x^{1/3} + 2$ . Then, the scattering efficiency ( $Q_{sca}$ ), extinction efficiency ( $Q_{ext}$ ) and asymmetry parameter ( $g$ ) [34] can be calculated as follows:

$$Q_{sca} = \frac{2}{x^2} \sum_{i=1}^{i_{max}} (2i+1)(|a_i|^2 + |b_i|^2), \quad (2)$$

$$Q_{ext} = \frac{2}{x^2} \sum_{i=1}^{i_{max}} (2i+1)Re[a_i + b_i], \quad (3)$$

$$\begin{aligned} g &= \frac{4}{x^2 Q_{sca}} \left[ \sum_{i=1}^{i_{max}} \frac{i(i+2)}{(2i+1)} Re(a_i a_{i+1}^* + b_i b_{i+1}^*) \right. \\ &\quad \left. + \sum_{i=1}^{i_{max}} \frac{(2i+1)}{i(i+1)} Re(a_i b_i^*) \right]. \end{aligned} \quad (4)$$

The absorption efficiency is calculated as:  $Q_{abs} = Q_{ext} - Q_{sca}$ .

The nanocomposite of air-calcite with  $w$  multiple particle diameters is approximated as an effective medium, and the total effective scattering ( $\sigma_\lambda$ ) and absorption ( $\kappa_\lambda$ ) coefficients, and asymmetry parameter ( $g_\lambda$ ) at each distinct wavelength  $\lambda$  is given as [35]:

$$\sigma_\lambda = \sum_{k=1}^w \frac{3 \phi_k Q_{sca,k}}{2d_k}, \quad \kappa_\lambda = \sum_{k=1}^w \frac{3 \phi_k Q_{abs,k}}{2d_k}, \quad g_\lambda = \frac{1}{\sigma_\lambda} \sum_{k=1}^w \frac{3 \phi_k g_k Q_{sca,k}}{2d_k}, \quad (5)$$

where  $\phi$  is the nanoparticle volume fraction,  $\sigma_T$  is the total scattering coefficient for all the other sizes. Finally, the particles' scattering is considered dependent at high volume fraction  $\phi > 10\%$ . Thus, a dependent scattering correction  $\sigma_{T,d}$  is added to the model [36]:

$$\sigma_{T,d} = \sigma_T (1 + 1.5\phi_T - 0.75\phi_T^2). \quad (6)$$

Similarly, the dependent absorbing correction  $\kappa_{T,d}$  is given:

$$\kappa_{T,d} = \kappa_T (1 + 1.5\phi_T - 0.75\phi_T^2). \quad (7)$$

### 2.2. Monte Carlo simulation

Monte Carlo simulation uses the optical properties calculated by Mie theory, and then, by assuming the composite as an effective medium, it predicts the spectral response of the nanocomposite. The Monte Carlo simulation solves stochastically the radiative transfer equation (RTE) combined with the top and bottom boundary conditions and plane periodic boundary conditions. The equation shows how a photon travels within the nanocomposite. Each distinct photon can be reflected, transmitted, or absorbed (if the media is lossy), as shown in Fig. 1(c). The RTE equation is given below [34,37]:

$$\frac{dI_\lambda}{ds} = \kappa_{T,\lambda} I_{b,\lambda} - (\sigma_{T,\lambda} + \kappa_{T,\lambda}) I_\lambda + \frac{\sigma_{T,\lambda}}{4\pi} \int_{4\pi} I_\lambda(\hat{s}_i) \Phi_{T,\lambda}(\hat{s}_i, \hat{s}) d\Omega_i, \quad (8)$$

where  $I_\lambda$  is the light intensity at specific  $\lambda$ ,  $\hat{s}$  is the unit vector and  $\Phi_{T,\lambda}$  is the phase function of averaged particle's sizes. The phase function of a single nanoparticle is given:

$$\Phi(\theta) = 2 \frac{|S_1|^2 + |S_2|^2}{x^2 Q_{sca}}. \quad (9)$$

The terms  $S_1$  and  $S_2$  are the scattering amplitudes related to the light polarization, and their calculation is well explained in previous literature [38]. In the end, the Monte Carlo simulation provides the values of the spectral reflectance  $R(\lambda)$ , emissivity  $\epsilon(\lambda)$ , and transmissivity  $T(\lambda)$ .

### 2.3. Transfer Matrix Method (TMM)

The nanolayered system's reflectance, transmittance, and absorptance (illustrated in Fig. 1(b)) are determined through the TMM. This method entails an analytical formulation tailored for 1D systems, relying on Maxwell's equations within an electric field context [20,39]. We

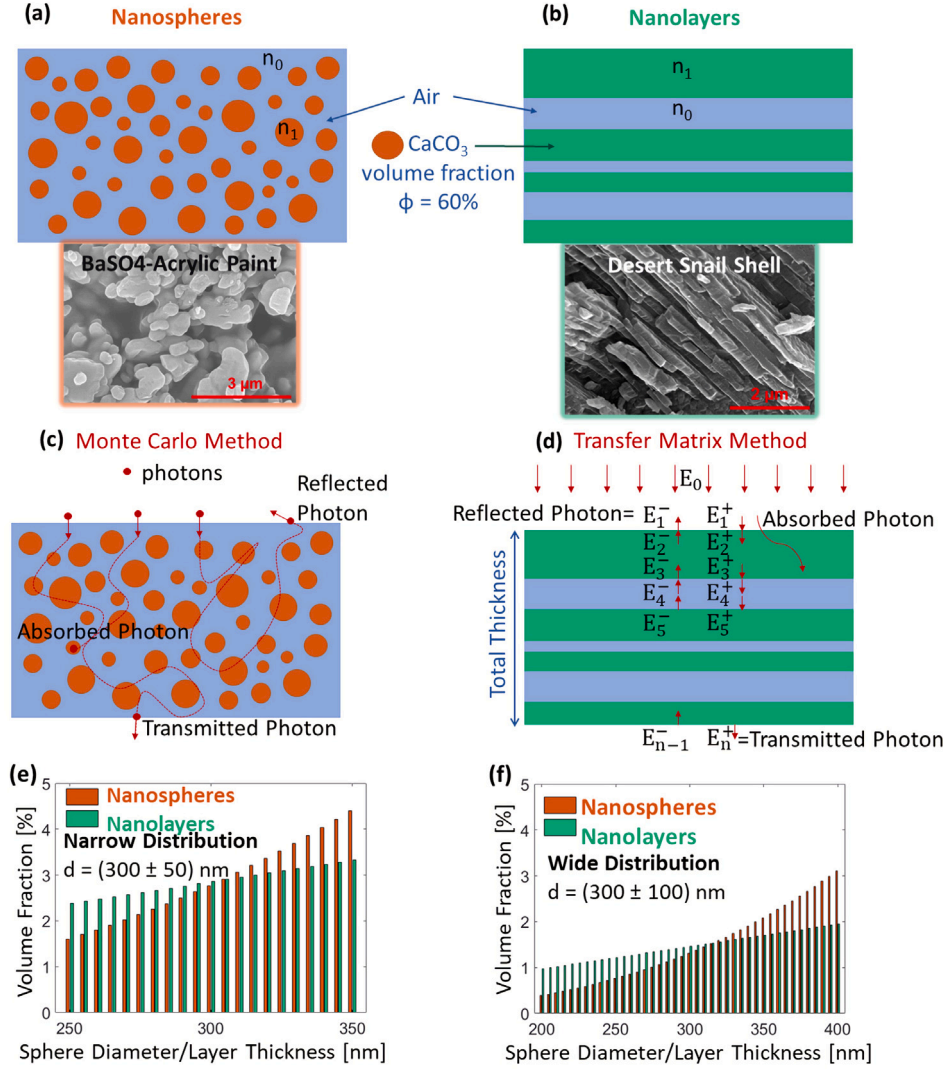


**Fig. 1.** Schematics and methods of 3D nanospheres vs. 1D nanolayers. (a) Calcite nanospheres (orange) dispersed in the air (blue) and an SEM image of barium sulfate ( $\text{BaSO}_4$ )-Acrylic paint, demonstrating spherical nanoparticle morphology in a polymer matrix. (b) Nanolayers of calcite (green) and air (blue), and an SEM image of calcium carbonate layers naturally occurring in *Sphincterochila zonata* desert snails. The spectral response of (c) the nanospheres is obtained via Monte Carlo simulation, and (d) for the nanolayers is calculated via TMM. (e) Volume fraction vs. distinct sphere diameter and layer thickness of narrow distribution. Variability is  $300 \text{ nm} \pm 50 \text{ nm}$ . (f) The corresponding volume fraction of the wide distribution, the variability is defined as  $300 \text{ nm} \pm 100 \text{ nm}$ . (For interpretation of the references to color in this figure legend, the reader is referred to the web version of this article.)

assume ideal interfacial characteristics in the calcite-air multilayer system, devoid of interfacial roughness. Consequently, the incident electric field  $E_0$  experiences uniform reflection and transmission through the multilayer, resulting in forward ( $E_i^+$ ) and backward ( $E_i^-$ ) components at each interface ( $i$ ), as depicted in Fig. 1(d). We calculate the electric field components for the initial layer using the following transfer matrix formulation [20]:

$$\begin{bmatrix} E_1^+ \\ E_1^- \end{bmatrix} = \begin{bmatrix} \frac{n_0 + n_1}{2n_1} & \frac{n_0 - n_1}{2n_1} \\ \frac{n_0 - n_1}{2n_1} & \frac{n_0 + n_1}{2n_1} \end{bmatrix} \begin{bmatrix} E_2^+ \\ E_2^- \end{bmatrix} = T_{1 \rightarrow 2} \begin{bmatrix} E_2^+ \\ E_2^- \end{bmatrix}, \quad (10)$$

$$\begin{bmatrix} E_2^+ \\ E_2^- \end{bmatrix} = \begin{bmatrix} e^{j k_1 d_1} & 0 \\ 0 & e^{-j k_1 d_1} \end{bmatrix} \begin{bmatrix} E_3^+ \\ E_3^- \end{bmatrix} = S_{2 \rightarrow 3} \begin{bmatrix} E_3^+ \\ E_3^- \end{bmatrix}. \quad (11)$$

In these equations,  $d_1$  represents the thickness of the first layer. For wavelengths within the sky window spectrum, the complex refractive index of calcite accounts for its absorption properties  $\tilde{n}_1 = n_1 + i\kappa_1$ . The wave number  $k_1$  is given by  $k_1 = \frac{2\pi n_1}{\lambda_0}$ , where  $\lambda_0$  is the vacuum wavelength. The general expressions in Eqs. (10) and (11) apply to any  $i$  interface and  $w$  layers, where  $w$  represents the total number of layers.

The resulting electric field components for  $n$  layers are obtained as:

$$\begin{bmatrix} E_1^+ \\ E_1^- \end{bmatrix} = T_{1 \rightarrow 2} S_{2 \rightarrow 3} T_{3 \rightarrow 4} \dots S_{n-2 \rightarrow n-1} T_{n-1 \rightarrow n} \begin{bmatrix} E_n^+ \\ 0 \end{bmatrix}, \quad (12)$$

where  $E_n^+ = E_t$  is the transmitted component of the incident electric field. Consequently, the reflected electric field is computed as  $E_r = E_1^-$ . Subsequently, the multilayer's transmissivity  $T(\lambda)$  and reflectivity  $R(\lambda)$  are determined by:

$$T(\lambda) = \left| \frac{E_t}{E_0} \right|^2, \quad (13)$$

$$R(\lambda) = \left| \frac{E_r}{E_0} \right|^2. \quad (14)$$

The spectral emissivity  $\epsilon(\lambda)$  is then calculated using:

$$\epsilon(\lambda) = 1 - R(\lambda) - T(\lambda). \quad (15)$$

Coherent interactions are observed in TMM for periodic and aperiodic structures with smooth interfaces, resulting in constructive and destructive interference at some wavelengths in the spectrum. A new

thickness profile introduces randomness, which is generated using a random number array normalized by its standard deviation while maintaining the total thickness and average layer thickness constant [39]:

$$d_i = d_0 + \Delta x \hat{X}_i, \quad (16)$$

where  $d_i$  is the new layer thickness for  $i$ th layer,  $d_0$  is the original layer thickness,  $\Delta x$  is the degree of randomness, and  $\hat{X}_i$  is a random number in the range  $(-1,1)$  generated for the  $i$ th layer. This randomization process is applied separately to the calcite and air gap layers while maintaining the desired volume fraction.

The randomized structure has a large number of relocalizations and to obtain the statistical average we iterate the process such that the spectral transmissivity and reflectance values are averaged over a designated number of iterations (typically around 10,000 repetitions). This approach yields a transfer matrix code with randomness inclusion, which is employed in this study to address the effects of coherence. Wide and narrow distributions are considered by varying the maximum randomness values to explore different scenarios.

#### 2.4. Solar reflection

The total solar reflectance is calculated from the spectral reflectance  $R(\lambda)$  by integrating across the solar irradiation spectrum. The incident solar radiation spectrum considered in this work is the Air Mass 1.5 (AM1.5) solar spectra by ASTM standards [40]. The AM1.5 irradiation ( $G_{solar,AM1.5}(\lambda)$ ) represents the solar radiation under standard conditions and is used for performing the weighted integration of spectral reflectance as shown below:

$$R_{total} = \frac{\int_{0.25 \mu m}^{2.5 \mu m} R(\lambda) G_{solar,AM1.5}(\lambda) d\lambda}{\int_{0.25 \mu m}^{2.5 \mu m} G_{solar,AM1.5}(\lambda) d\lambda}. \quad (17)$$

#### 2.5. Sky window emissivity

Similarly, the total sky window emissivity  $\epsilon_{sky}$  is calculated based on the overall radiation emissivity by the composites into deep space in the atmospheric transmittance window, using the blackbody radiation at room temperature. This is shown in the equation below [41]:

$$\epsilon_{sky} = \frac{\int_{8 \mu m}^{13 \mu m} \epsilon(\lambda) I_{BB,300 K}(\lambda) d\lambda}{\int_{8 \mu m}^{13 \mu m} I_{BB,300 K}(\lambda) d\lambda}, \quad (18)$$

where  $I_{BB,300 K}(\lambda)$  is the blackbody radiation intensity at room temperature ( $T = 300$  K), which is calculated using the Planck radiation law as shown in the equation below:

$$I_{BB,T}(\lambda) = \frac{2\pi hc^2}{\lambda^5} \frac{1}{\exp\left(\frac{hc}{k_b \lambda T}\right) - 1}. \quad (19)$$

Here  $h$  and  $k_b$  are Planck's and Boltzmann's constants, and  $c$  is the speed of light.

#### 2.6. Figure of merit

The figure of merit ( $RC$ ) provides a comprehensive measure of a composite's radiative cooling performance, taking into account its ability to radiate heat to the sky while minimizing solar heat absorption, and is defined as follows [10]:

$$RC = \epsilon_{sky} - r(1 - R_{total}), \quad (20)$$

where  $r$  is the ratio of the total reflectance over the blackbody emissivity.

**Table 1**

Inputs of the models.

Total volume fraction	60%
Size (d)	100–1100 nm
Narrow distribution	$d \pm 15\% d$
Wide distribution	$d \pm 30\% d$
Total film thickness	2–200 $\mu m$
Number of Photons for Monte Carlo	500,000
Number of iterations for multilayers	10,000

#### 2.7. Model's inputs

To ensure a meaningful comparison, we have maintained a constant total volume fraction of 60%, as previous experiments have shown that a high concentration of nanoparticles can enhance the total reflectance [4,10]. The characteristic length (sphere diameter and layer thickness) with a uniform size distribution remains consistent across both models. The refractive index of calcite employed in our models has been determined through prior experiments and calculations tailored explicitly for the solar spectrum Ref. Ghosh [42] and the sky window [43]. A comprehensive summary of all input parameters and material properties is condensed in Table 1.

Two uniform size distributions are considered to include randomness, the narrow ( $d = 300 \pm 50$  nm) and wide ( $d = 300 \pm 100$  nm) distributions. The difference in volume fraction distributions between the two structures arises from the fundamental scaling principles of 1D and 3D systems (Fig. 1(e)–(f)). The volume scales linearly with layer thickness in a 1D system, such as the nanolayers considered here. Contrastingly, in a 3D system, like the spherical nanoparticles, the volume scales with the cube of the diameter. As a result, to maintain a constant total volume fraction of calcite within the composite, the size distribution of nanospheres needs to be adjusted differently compared to the nanolayers. This inherent difference in scaling between 1D and 3D systems leads to distinct volume fraction distributions, which, in turn, influence the composites' optical properties and radiative performance.

### 3. Results and discussion

The resulting coating solar reflectance versus the total thickness for the narrow and wide distributions is shown in Fig. 2(a) and (b), respectively. As expected, both morphologies show a gradually plateauing total reflectance. For the narrow distribution, this plateau occurs at around 40  $\mu m$  of total thickness for both nanospheres and nanolayers. However, in the case of the wide distribution, nanolayers exhibit an overall performance improvement over compared to narrow distribution, reaching a higher reflectance than nanospheres at film thicknesses bigger than 15  $\mu m$ . Beyond this thickness, the reflectance of both nanolayers and nanospheres plateaus. The maximum total reflectance achieved at 100  $\mu m$  for nanolayers is 99.85%, and for nanospheres 98.53% in the wide distribution.

The sky window emissivity of the two structures is also calculated and given in Fig. 2(c) and 2(d). Nanolayers exhibit up to 6% higher emissivity than nanospheres, which can be attributed to the coherency part of the TMM (detailed explanation provided in Fig. S1). Sky window emissivity, unlike reflectance, shows only slight sensitivity to the size distribution of the particles. Additionally, it is worth noting that sky window emissivity remains relatively constant across different sizes (Fig. S2). This can be easily explained due to the Rayleigh scattering that occurs when the wavelengths are at least ten times larger than the nanoparticle's diameter.

In Fig. 3, we delve into the coatings' behavior by examining their wavelength-dependent reflectance (Fig. 3(a)–(b)) and emissivity (Fig. 3(c)–(d)) at specific coating thicknesses of 100 and 20  $\mu m$ . For the nanospheres, we observe consistently high reflectance in the ultraviolet (UV) and visible (Vis) regimes, with a declining trend in the near-infrared (NIR) wavelengths across all cases. Notably, the distribution

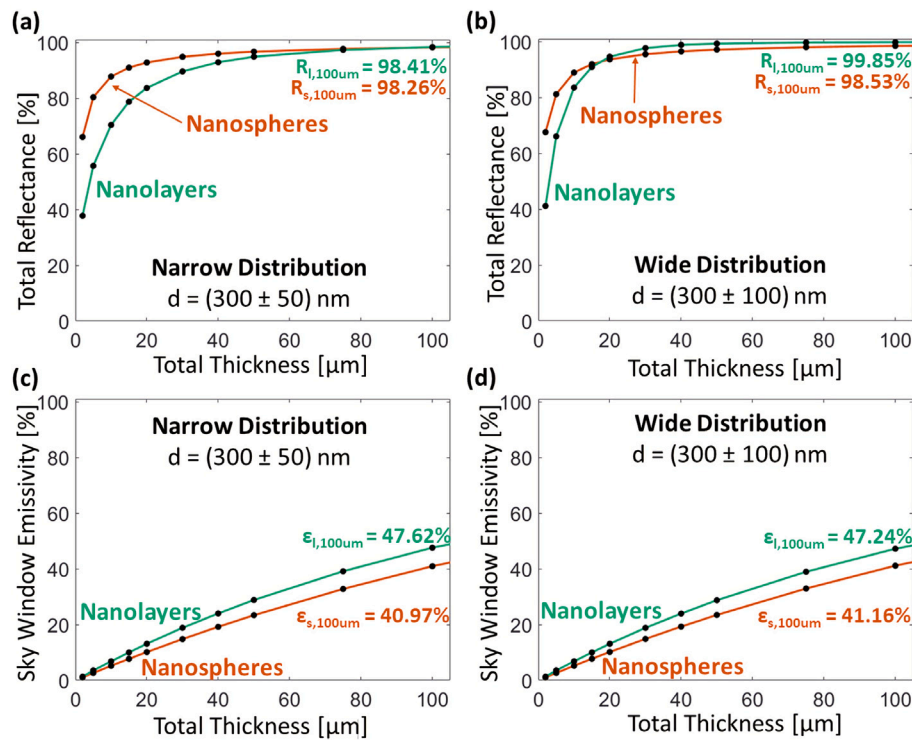


Fig. 2. Radiative cooling performance comparison for nanospheres and nanolayers with average size of 300 nm. (a) The total reflectance vs. the total film thickness of the narrow and (b) the wide distributions. (c) The sky window emissivity vs. the total film thickness of the narrow and (d) wide distributions.

predominantly influences the response at NIR wavelengths, with wider distributions meaning bigger particles are included in the composite, higher scattering is expected particularly at longer wavelengths compared to smaller particles. The higher scattering results in an exhibiting enhanced overall performance. Switching from a wide to a narrow distribution for nanospheres results in a slight decrease in total reflectance from 98.53% to 98.26% for a 100 μm thickness coating and from 93.68% to 92.82% for a 20 μm coating.

Reflectance in nanolayer medium is accounted for photon localization in the multilayer system [20,21]. We observe that using a wide distribution increases the photon localization in the valley regions observed in the spectral reflectance, which leads to a higher solar reflectance. In wide distribution, we consider multilayer systems with more deviations in the layer thicknesses, this helps localize the photons that are not localized in the narrow distribution. Consequently, nanolayers with wide distributions outperform their narrow distribution counterparts in terms of total reflectance. For instance, at a thickness of 100 μm, total reflectance experiences a reduction of approximately 1.4%, whereas a notably more significant decrease of about 11% is observed at 20 μm, switching from wide to narrow distribution.

The spectral emissivity (Fig. 3(c)–(d)) within the 8–13 μm wavelength range, shows a declining trend at longer wavelengths for both structures. Notably, size distribution has negligible impact, as spectral absorptance remains consistent. Nanolayer spectral emissivity is higher than nanospheres in all the wavelengths. However, thicker film coatings exhibit a more significant difference in sky window emissivity between the two morphologies, with an increase of approximately 6% at 100 μm and 3% at 20 μm.

Furthermore, we evaluate the coatings' radiative cooling performance through the figure of merit (RC), a key metric that quantifies their ability to achieve sub-ambient temperatures by radiating excess heat into space, (i.e., RC is greater than zero). The results presented in Fig. 3(e) provide insights into the overall cooling performance of these coatings and their potential practical applications. Notably, nanolayers

with a wide distribution achieve the highest RC value of 0.68 at a total thickness of 200 μm, requiring a coating thickness exceeding 32 μm for sub-ambient cooling. In contrast, nanolayers with a narrow distribution exhibit an RC of 0.64 but necessitate a more substantial coating thickness, exceeding 66 μm, for sub-ambient cooling. Nanospheres, whether with a wide or narrow distribution, achieve RC values of 0.57 and 0.55, respectively, with minimum coating thickness requirements of 56 μm and 62 μm for sub-ambient cooling.

We repeat the same calculations to analyze further the total reflectance performance for smaller ( $d = 100$  nm) and larger ( $d = 500$  nm) average sizes. At 100 nm and narrow distribution, the total reflectance of nanolayers and nanospheres nearly coincides, and the total reflectance of the nanolayered structure is greater by only 2% (Fig. 4(a)). However, nanolayers perform significantly better in the wide distribution system than the nanospheres, with an 8% difference (Fig. 4(b)). This indicates that a wide distribution of layer thicknesses helps the multilayer reflection. Interestingly, the nanospheres with an averaged characteristic length of 500 nm show much better performance in both cases, i.e., narrow (Fig. 4(c)) and wide (Fig. 4(d)) distributions. However, the gap between layers' performance and particles is minimized in wide distribution. Additionally, we note that at 500 nm average size, the nanosphere coatings plateau relatively faster with increasing thickness as compared to nanolayers of the same average size as well as nanospheres of 100 nm and 300 nm. This indicates that larger nanospheres are suitable for enhancing total reflectance due to the Mie scattering that occurs. However, the plateauing trend is not readily observable in nanolayers, even at a higher total thickness of greater than 100 μm. Thus indicating a significant difference in behavior to nanospheres of the same material and size.

In order to further understand the effect of average particle and layer size, we analyzed the trend of total reflectance by varying the average particle and layer size for two fixed total thickness values of 20 and 100 μm (Fig. 5) Initially, the total reflectance increases sharply with an increase in size, and the nanolayers perform better in this case than the nanospheres. The nanolayers' optimal size is

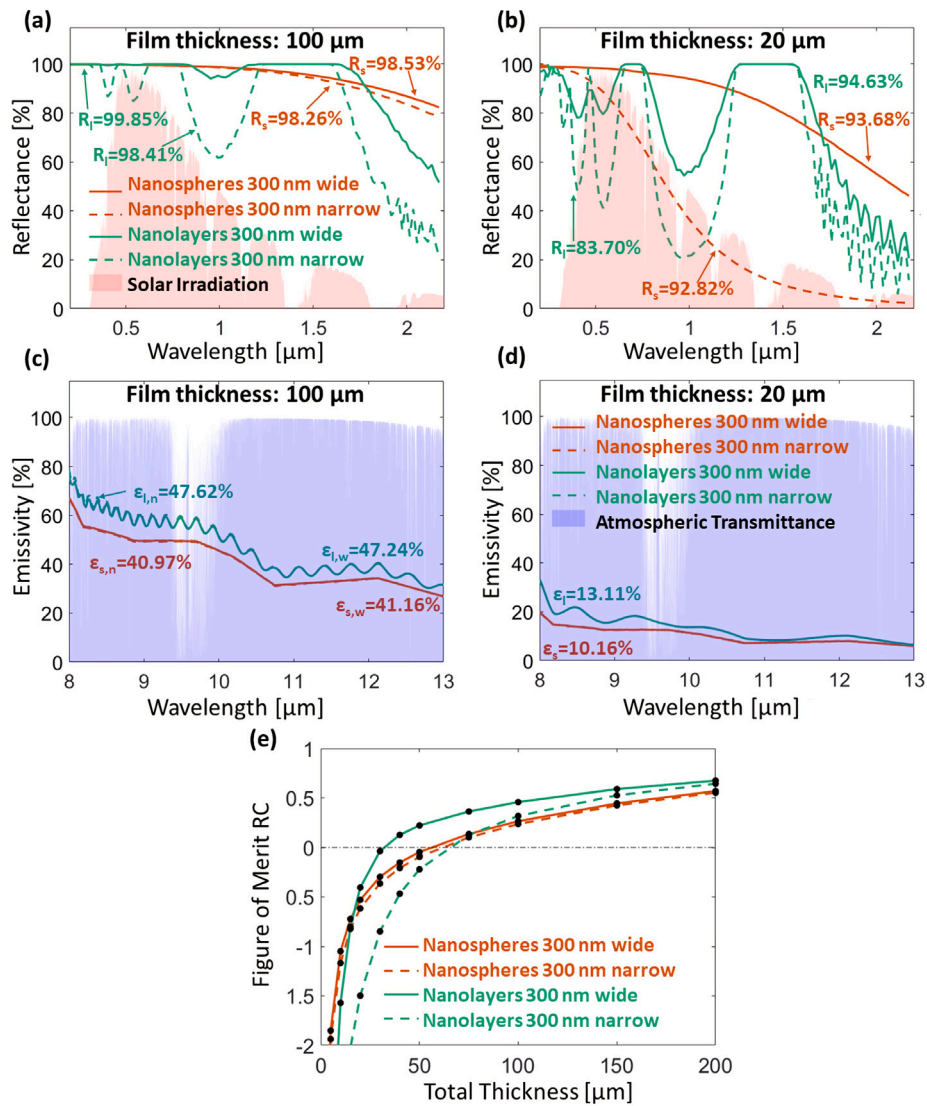


Fig. 3. Spectral response for spheres and layers average size of 300 nm. (a) The spectral reflectance of nanospheres and nanolayers for 100 μm film thickness. Solid and dashed lines represent the wide and narrow distributions, respectively. (b) The spectral reflectance of nanospheres and nanolayers for 20 μm film thickness. (c) Sky window emissivity of coating thickness of 100 μm and (d) 20 μm. (e) The Figure of merit vs. the total coating thickness.

around 300 nm, while the nanospheres' optimal size ranges from 500 to 600 nm. Moreover, increasing particle size results in a gradual decrease in total reflectance. This behavior is significantly distinct from that of nanolayers, which shows a steep drop to the total reflectance of about 60% at 700 nm average calcite layer thickness. The difference of total reflectance at 20 μm total thickness is about 35% at 700 nm average size.

Notably, the optimized nanolayer structure has a smaller characteristic length than nanospheres. The difference comes from the structures' distinct reflection mechanisms. The nanospheres' system relies on the multiple scattering events of photons on the particles. It is well known that the maximum reflectance occurs when the sphere diameter is equal to the wavelength, also known as Mie scattering. Mie scattering is favored for spherical nanoparticles due to their high scattering coefficient, resulting in stronger backscattering compared to Geometric and Rayleigh scattering, despite unfavorable asymmetry parameter [11,35]. In contrast, multilayered structures are known for confining photons due to the interference of the transmitted and reflected electric fields within the layer. The localization behavior is a known and studied phenomenon in multilayer structures [20,21].

RC was also calculated for various nanoparticle sizes and is summarized in Table 2, with a constant coating thickness of 100 μm

**Table 2**  
Figure of merit RC of different sizes at a constant total coating thickness of 100 μm.

Size	100 nm	300 nm	500 nm	700 nm
Nanolayers	0.013	0.457	-0.310	-0.800
Nanospheres	-1.142	0.265	0.358	0.393

across all composites. The highest RC value, 0.46, was attained by nanolayers with an average size of 300 nm. For other sizes, nanolayers exhibited either negative or negligible RC values due to their low total reflectance. In contrast, nanospheres achieved positive RC values for several size variations ranging from 300 to 700 nm in diameter. The maximum RC value for nanospheres was 0.39, observed at a diameter of 700 nm. Although nanolayers have the highest performance at optimal sizes, nanospheres have robust performance across a wide range of particle sizes.

#### 4. Conclusion

In this study, we have compared two distinct structural configurations within calcite-air composites, nanolayers, and nanospheres,

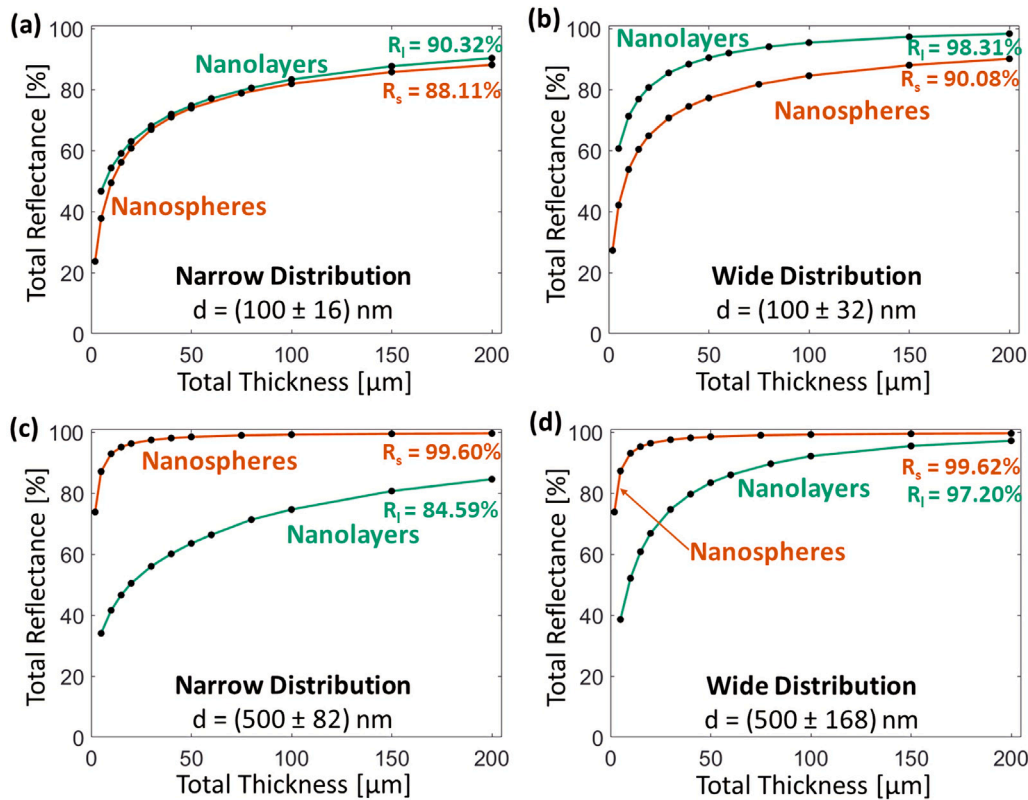


Fig. 4. Total reflectance of both structures at different characteristic lengths. (a) Narrow and (b) wide distributions with an average diameter and thickness of 100 nm. (c) Narrow and (d) wide distributions with a 500 nm average characteristic length.

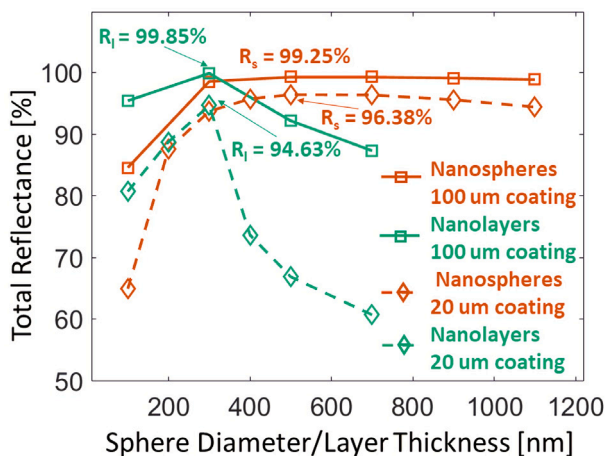


Fig. 5. Different structures optimize at different characteristic lengths. The nanolayer structure performs better at smaller sizes compared to nanospheres. For thicker coatings, like 100 μm, nanolayers achieve the highest total reflectance of 99.85% with an average layer thickness of 300 nm and a wide distribution. In contrast to nanospheres, at 500 nm diameter, the reflectance maximizes at 99.25%. For thinner coatings, like 20 μm, nanospheres reach up to 96.38%, and nanolayers are maximized at 94.63%.

to determine the optimal design for achieving high radiative cooling performance. To comprehensively assess the overall radiative performance, we utilized the figure of merit RC that requires the calculation of the total reflectance and sky window emissivity. Surprisingly, nanolayers achieved the highest radiative cooling performance, boasting an RC value of 0.457, characterized by an average size of 300 nm

and a total coating thickness of 100 μm. Each structure has different optimization sizes, with nanolayers optimizing at 300 nm average layer thickness and achieving an ultrahigh reflectance of 99.85% at only 100 μm total film thickness. On the other hand, nanospheres offer an optimal solar reflectance of 99.25% at 100 μm total thickness and 500 nm diameter size with wide distribution. Further analysis showed that the distribution positively influences nanolayered structure by providing broader-band reflection across the solar spectrum. However, the impact of distribution is limited in particles, showing only a slight enhancement in wide distribution compared to the narrow distribution. These results show a clear distinction in the way the two morphologies behave. Sky window emissivity was systematically evaluated in our study. Nanolayers demonstrated a higher emissivity, exhibiting an increase of up to approximately 6% when compared to nanoparticles. Its consistency across different sizes and size distributions sets sky window emissivity apart from total reflectance.

Our observation that layers perform better than nanospheres is not absolute. It differs based on multiple factors, such as particle/layer size, size distribution in the system, and the total thickness of the coating. This comparative study is impactful in designing more efficient ultra-reflective films by making a wise choice of morphology and size for that specific geometry.

**CRedit authorship contribution statement**

**Ioanna Katsamba:** Writing – original draft, Methodology, Investigation, Conceptualization. **Krutarth Khot:** Writing – review & editing, Writing – original draft, Methodology, Investigation, Conceptualization. **Andrea Felicelli:** Writing – review & editing, Visualization, Methodology. **Xiulin Ruan:** Writing – review & editing, Supervision, Methodology, Conceptualization.

## Declaration of competing interest

The authors declare the following financial interests/personal relationships which may be considered as potential competing interests: The authors have no known competing financial interests or personal relationships that could have appeared to influence the work reported in this paper.

## Data availability

Data will be made available on request.

## Acknowledgments

The authors acknowledge Dr. Dudong Feng for reviewing the text. I.K. and X.R. acknowledge support from the US National Science Foundation through award 2102645. A.F. acknowledges partial support from the US National Science Foundation through a Graduate Research Fellowship.

During the preparation of this work, the authors used ChatGPT and Grammarly in order to polish and improve language. After using this tool, the authors reviewed and edited the content as needed and took full responsibility for the content of the publication.

## Appendix A. Supplementary data

Supplementary material related to this article can be found online at <https://doi.org/10.1016/j.ijheatmasstransfer.2024.125902>.

## References

- [1] S. Catalanotti, V. Cuomo, G. Piro, D. Ruggi, V. Silvestrini, G. Troise, The radiative cooling of selective surfaces, *Solar Energy* 17 (2) (1975) 83–89, [http://dx.doi.org/10.1016/0038-092X\(75\)90062-6](http://dx.doi.org/10.1016/0038-092X(75)90062-6).
- [2] A. Harrison, M. Walton, Radiative cooling of TiO<sub>2</sub> white paint, *Sol. Energy* 20 (2) (1978) 185–188, [http://dx.doi.org/10.1016/0038-092X\(78\)90195-0](http://dx.doi.org/10.1016/0038-092X(78)90195-0).
- [3] A.P. Raman, M.A. Anoma, L. Zhu, E. Rephaeli, S. Fan, Passive radiative cooling below ambient air temperature under direct sunlight, *Nature* 515 (7528) (2014) 540–544, <http://dx.doi.org/10.1038/nature13883>.
- [4] X. Li, J. Peoples, Z. Huang, Z. Zhao, J. Qiu, X. Ruan, Full daytime sub-ambient radiative cooling in commercial-like paints with high figure of merit, *Cell Rep. Phys. Sci.* (2020) 100221, <http://dx.doi.org/10.1016/j.xcrp.2020.100221>.
- [5] B. Orel, M. Gunde, A. Krainer, Radiative cooling efficiency of white pigmented paints, *Sol. Energy* 50 (6) (1993) 477–482, [http://dx.doi.org/10.1016/0038-092X\(93\)90108-Z](http://dx.doi.org/10.1016/0038-092X(93)90108-Z).
- [6] J.-I. Kou, Z. Jurado, Z. Chen, S. Fan, A.J. Minnich, Daytime radiative cooling using near-black infrared emitters, *ACS Photonics* 4 (3) (2017) 626–630, <http://dx.doi.org/10.1021/acsp Photonics.6b00991>.
- [7] Y. Zhai, Y. Ma, S.N. David, D. Zhao, R. Lou, G. Tan, R. Yang, X. Yin, Scalable-manufactured randomized glass-polymer hybrid metamaterial for daytime radiative cooling, *Science* 355 (6329) (2017) 1062–1066, <http://dx.doi.org/10.1126/science.aai7899>.
- [8] T. Li, Y. Zhai, S. He, W. Gan, Z. Wei, M. Heidarnejad, D. Dalgo, R. Mi, X. Zhao, J. Song, J. Dai, C. Chen, A. Aili, A. Vellore, A. Martini, R. Yang, J. Srebric, X. Yin, L. Hu, A radiative cooling structural material, *Science* 364 (6442) (2019) 760–763, <http://dx.doi.org/10.1126/science.aau9101>.
- [9] E. Rephaeli, A. Raman, S. Fan, Ultrabroadband photonic structures to achieve high-performance daytime radiative cooling, *Nano Lett.* 13 (4) (2013) 1457–1461, <http://dx.doi.org/10.1021/nl4004283>.
- [10] X. Li, J. Peoples, P. Yao, X. Ruan, Ultrawhite BaSO<sub>4</sub> paints and films for remarkable daytime subambient radiative cooling, *ACS Appl. Mater. Interfaces* 13 (2021) 21733–21739, <http://dx.doi.org/10.1021/acsaami.1c02368>.
- [11] A. Felicelli, I. Katsamba, F. Barrios, Y. Zhang, Z. Guo, J. Peoples, G. Chiu, X. Ruan, Thin layer lightweight and ultrawhite hexagonal boron nitride nanoporous paints for daytime radiative cooling, *Cell Rep. Phys. Sci.* 3 (10) (2022) 101058, <http://dx.doi.org/10.1016/j.xcrp.2022.101058>.
- [12] N.N. Shi, C.-C. Tsai, F. Camino, G.D. Bernard, N. Yu, R. Wehner, Keeping cool: Enhanced optical reflection and radiative heat dissipation in Saharan silver ants, *Science* 349 (6245) (2015) 298–301, <http://dx.doi.org/10.1126/science.aab3564>.
- [13] S. Lin, L. Ai, J. Zhang, T. Bu, H. Li, F. Huang, J. Zhang, Y. Lu, W. Song, Silver ants-inspired flexible photonic architectures with improved transparency and heat radiation for photovoltaic devices, *Sol. Energy Mater. Sol. Cells* 203 (2019) 110135, <http://dx.doi.org/10.1016/j.solmat.2019.110135>.
- [14] H. Zhang, K.C.S. Ly, X. Liu, Z. Chen, M. Yan, Z. Wu, X. Wang, Y. Zheng, H. Zhou, T. Fan, Biologically inspired flexible photonic films for efficient passive radiative cooling, *Proc. Natl. Acad. Sci.* 117 (26) (2020) 14657–14666, <http://dx.doi.org/10.1073/pnas.2001802117>.
- [15] J. Lee, Y. Jung, M. Lee, J.S. Hwang, J. Guo, W. Shin, J. Min, K.R. Pyun, H. Lee, Y. Lee, J. Shiomi, Y.-J. Kim, B.-W. Kim, S.H. Ko, Biomimetic reconstruction of butterfly wing scale nanostructure for radiative cooling and structural coloration, *Nanoscale Horiz.* 7 (2022) <http://dx.doi.org/10.1039/d2nh00166g>.
- [16] K. Schmidt-Nielsen, C.R. Taylor, A. Shkolnik, Desert snails: problems of heat, water and food, *J. Exp. Biol.* 55 (2) (1971) 385–398, <http://dx.doi.org/10.1242/jeb.55.2.385>.
- [17] W. Gellermann, M. Kohmoto, B. Sutherland, P.C. Taylor, Localization of light waves in Fibonacci dielectric multilayers, *Phys. Rev. Lett.* 72 (1994) 633, <http://dx.doi.org/10.1103/PhysRevLett.72.633>.
- [18] E. Yablonovitch, Engineered omnidirectional external-reflectivity spectra from one-dimensional layered interference filters, *Opt. Lett.* 23 (1998) <http://dx.doi.org/10.1364/ol.23.001648>.
- [19] J.N. Winn, Y. Fink, S. Fan, J.D. Joannopoulos, Omnidirectional reflection from a one-dimensional photonic crystal, *Opt. Lett.* 23 (1998) <http://dx.doi.org/10.1364/OL.23.001573>.
- [20] X.L. Ruan, M. Kaviany, Photon localization and electromagnetic field enhancement in laser-irradiated, random porous media, *Microsc. Thermophys. Eng.* (2005) 63–84, <http://dx.doi.org/10.1080/10893950590913404>.
- [21] J.D. Joannopoulos, S.G. Johnson, J.N. Winn, R.D. Meade, *Photonic Crystals: Molding the Flow of Light*, Princeton University Press, 2011, <http://dx.doi.org/10.2307/j.ctvcn4gz9>.
- [22] K. Yao, H. Ma, M. Huang, H. Zhao, J. Zhao, Y. Li, S. Dou, Y. Zhan, Near-perfect selective photonic crystal emitter with nanoscale layers for daytime radiative cooling, *ACS Appl. Nano Mater.* (2019) 5512–5519, <http://dx.doi.org/10.1021/acsaanm.9b01097>.
- [23] D. Chae, M. Kim, P.H. Jung, S. Son, J. Seo, Y. Liu, B.J. Lee, H. Lee, Spectrally selective inorganic-based multilayer emitter for daytime radiative cooling, *ACS Appl. Mater. Interfaces* 12 (2020) 8073–8081, <http://dx.doi.org/10.1021/acsaami.9b16742>.
- [24] Y. Zhu, Y.H. Ye, D. Wang, Y. Cao, Quasi-periodic selective multilayer emitter for sub-ambient daytime radiative cooling, *AIP Adv.* 11 (2021) 025109, <http://dx.doi.org/10.1063/5.0035138>.
- [25] P. You, X. Li, Y. Huang, X. Ma, M. Pu, Y. Guo, X. Luo, High-performance multilayer radiative cooling films designed with flexible hybrid optimization strategy, *Materials* (2020) <http://dx.doi.org/10.3390/MA13132885>.
- [26] M. Kim, J. Seo, S. Yoon, H. Lee, J. Lee, B.J. Lee, Optimization and performance analysis of a multilayer structure for daytime radiative cooling, *J. Quant. Spectrosc. Radiat. Transfer* 260 (2021) <http://dx.doi.org/10.1016/j.jqsrt.2020.107475>.
- [27] G. Mabchour, M. Benlattar, K. Saadouni, M. Mazroui, Daytime radiative cooling purposes with selective multilayer design based on Ta<sub>2</sub>O<sub>5</sub>, *Optik* 214 (2020) 164811, <http://dx.doi.org/10.1016/J.IJLEO.2020.164811>.
- [28] K. Khot, P.R. Chowdhury, X. Ruan, Machine learning-based design optimization of aperiodic multilayer coatings for enhanced solar reflection, *Int. J. Heat Mass Transfer* 224 (2024) 125303, <http://dx.doi.org/10.1016/j.ijheatmasstransfer.2024.125303>.
- [29] P. Roy Chowdhury, K. Khot, J. Song, Z. He, D. Kortge, Z. Han, P. Bermel, H. Wang, X. Ruan, Machine learning designed and experimentally confirmed enhanced reflectance in aperiodic multilayer structures, *Adv. Opt. Mater.* 2300610 (2023) <http://dx.doi.org/10.1002/adom.202300610>.
- [30] C.F. Bohren, *Absorption and Scattering of Light by Small Particles*, Wiley-VCH Verlag GmbH & Co. KGaA, Weinheim, Germany, 2004, <http://dx.doi.org/10.1002/9783527618156>.
- [31] H.C.v.d. Hulst, *Light scattering by small particles*, Structure of Matter Series, Wiley, New York, 1957, <http://dx.doi.org/10.1002/qj.49708436025>.
- [32] M. Kerker, The Scattering of Light and Other Electromagnetic Radiation, in: Volume 16 in Physical Chemistry: A Series of Monographs, Academic Press, New York, 1969, <http://dx.doi.org/10.1016/c2013-0-06195-6>.
- [33] R. Salomão, L.M.M. Costa, G.M.d. Olyveira, Precipitated calcium carbonate nanoparticles: Applications in drug delivery, *Adv. Tissue Eng. Regen. Med.: Open Access* (2) (2017) <http://dx.doi.org/10.15406/atooa.2017.03.00059>.
- [34] M.F. Modest, *Radiative Heat Transfer*, Elsevier Science & Technology, San Diego, 2013, p. 391, <http://dx.doi.org/10.1016/c2010-0-65874-3>.
- [35] J. Peoples, X. Li, Y. Lv, J. Qiu, Z. Huang, X. Ruan, A strategy of hierarchical particle sizes in nanoparticle composite for enhancing solar reflection, *Int. J. Heat Mass Transfer* 131 (2019) 487–494, <http://dx.doi.org/10.1016/j.ijheatmasstransfer.2018.11.059>.
- [36] M. Kaviany, *Heat Transfer Physics*, Cambridge University Press, 2008, <http://dx.doi.org/10.1017/cbo9780511754586>.
- [37] J.R. Howell, M.P. Mengüç, K. Daun, R. Siegel, *Thermal Radiation Heat Transfer*, Taylor & Francis Group, Milton, 2020, <http://dx.doi.org/10.1201/9780429327308>.
- [38] Z. Huang, X. Ruan, Nanoparticle embedded double-layer coating for daytime radiative cooling, *Int. J. Heat Mass Transfer* 104 (2017) 890–896, <http://dx.doi.org/10.1016/j.ijheatmasstransfer.2016.08.009>.

- [39] C.C. Katsidis, D.I. Siapkas, General transfer-matrix method for optical multilayer systems with coherent, partially coherent, and incoherent interference, *Appl. Opt.* 41 (2002) 3978–3987, <http://dx.doi.org/10.1364/ao.41.003978>, Vol. 41, Issue 19, pp. 3978-3987.
- [40] ASTM, Standard tables for reference solar spectral irradiances: Direct normal and hemispherical on 37° tilted surface, *ASTM Int.* (2012) 1–21, <http://dx.doi.org/10.1520/G0173-03R12>.
- [41] C.G. Granqvist, A. Hjortsberg, Radiative cooling to low temperatures: General considerations and application to selectively emitting SiO films, *J. Appl. Phys.* 52 (6) (1981) 4205–4220, <http://dx.doi.org/10.1063/1.329270>.
- [42] G. Ghosh, Dispersion-equation coefficients for the refractive index and birefringence of calcite and quartz crystals, *Opt. Commun.* 163 (1) (1999) 95–102, [http://dx.doi.org/10.1016/S0030-4018\(99\)00091-7](http://dx.doi.org/10.1016/S0030-4018(99)00091-7).
- [43] C. Carteret, M. De La Pierre, M. Dossot, F. Pascale, A. Erba, R. Dovesi, The vibrational spectrum of CaCO<sub>3</sub> aragonite: A combined experimental and quantum-mechanical investigation, *J. Chem. Phys.* 138 (1) (2013) 014201, <http://dx.doi.org/10.1063/1.4772960>.